VECTOR FORM INTRINSIC FINITE ELEMENT BASED APPROACH TO SIMULATE CRACK PROPAGATION

Y. F. Duan **S. M. Wang**

College of Civil Engineering and Architecture
Zhejiang University
Hangzhou, China

R. Z. Wang*

National Center for Research on Earthquake Engineering
Taipei, Taiwan

C. Y. Wang

Department of Civil Engineering
National Central University
Taoyuan, Taiwan

E. C. Ting

School of Civil Engineering
Purdue University
West Lafayette, USA

ABSTRACT

This paper presents a new approach to simulate the propagation of elastic and cohesive cracks under mode-I loading based on the vector form intrinsic finite element method. The proposed approach can handle crack propagation without requiring global stiffness matrices and extra weak stiffness elements. The structure is simulated by mass particles whose motions are governed by the Newton's second law. Elastic and cohesive crack propagation are simulated by proposed VFIFE-*J*-integral and VFIFE-FCM methods, respectively. The VFIFE-*J*-integral method is based on vector form intrinsic finite element (VFIFE) and *J*-integral methods to calculate the stress intensity factors at the crack tips, and the VFIFE-FCM method combines VFIFE and fictitious crack models (FCM). When the stress state at the crack tip meets the fracture criterion, the mass particle at the crack tip is separated into two particles. The crack then extends in the plate until the plate splits into two parts. The proposed VFIFE-*J*-integral method was validated by elastic crack simulation of a notched plate, and the VFIFE-FCM method by cohesive crack propagation of a three point bending beam. As assembly of the global stiffness matrix is avoided and each mass particle motion is calculated independently, the proposed method is easy and efficient. Numerical comparisons demonstrate that the present results predicted by the VFIFE method are in agreement with previous analytical, numerical and experimental works.

Keywords: Crack propagation, VFIFIE-*J*-integral method, VFIFE-FCM method, Cohesive force.

1. INTRODUCTION

Linear elastic fracture mechanics (LEFM) has been available since 1920 by Grifftith [1]. Griffith fracture theory [1] is only applicable to elastic homogeneous brittle material, such as glass. According to Ewalds and Wanhill [2], Irwin [3] was the first to recognize the general applicability of the singular stress field and introduced the concept of the stress intensity factor (SIF) in LEFM to measure the strength of the singular stress field. LEFM is only applicable when the size of the fracture process zone (FPZ) at the crack tip is small compared to

* Corresponding author (rzwang@ncree.narl.org.tw)

DOI : 10.1017/jmech.2017.85
Copyright © 2017 The Society of Theoretical and Applied Mechanics
https://doi.org/10.1017/jmech.2017.85 Published online by Cambridge University Press

the size of the crack and specimen [4]. Other models must consider the FPZ [5]. Many crack models were proposed in the late 1970s, such as the theory of cohesive or fictitious cracking. For cohesive cracks, propagation is governed by a traction-displacement relation across the crack faces near the tip [5]. Hillerborg *et al*. [6] proposed the fictitious crack model (FCM) to analyze crack propagation in concrete. Hillerborg [7] introduced the concept of fracture energy into the FCM and proposed a number of traction–displacement relationships for concrete. Xu and Reinhardt [8] proposed the double-K fracture criterion to predict the crack propagation during the fracture process in quasi-brittle materials. The current paper introduces SIF and FCM into the VFIFE frame to simulate the linear and non-linear crack propagation.

Various numerical simulation methods have also been developed to investigate crack propagation. Since the early 1960s, the finite element method (FEM) has been applied to analyze concrete cracking [9]. The common way to deal with the crack problem is to adopt the embedded discontinuous model [10], the adaptive mesh method [11], and node force release method [12] to FEM. The introduction of those methods allows the FEM to solve the discontinuous problems while is still difficult to simulate the complex crack propagation. The boundary element method [13] and element free Galerkin method [14] have also widely used for discontinuous problem. However, boundary element method is difficult to deal with nonlinear problems and element free Galerkin method is hard to deal with boundary condition. Recently, some of the most developments in FEM modelling of crack propagation are based on the partition of unity [15, 16], including the generalized (G-FEM) [17], extended FEM (X-FEM) [18], and phantom node method (PNM) [19]. The G-FEM and X-FEM methods can deal with discontinuities by adding extra nodal degrees of freedom (DoF) and PNM by phantom nodes. The augmented FEM (A-FEM) [20] method uses the elemental condensation algorithm, and provides improved numerical accuracy, efficiency, and stability. However, all of these methods require internal nodal DoFs as functions of the external nodal DoFs for the cohesive laws when dealing with cohesive cracks. Since these methods are all in the finite element frame, solving the stiffness matrix becomes much more difficult with increasing DoFs. The displacement fields consist of continuous and discontinuous parts. Therefore, selecting shape functions to account for discontinuous crack displacements within an element is important but difficult, and additional sub-domain integration may be required for numerical calculations.

Previous numerical models were based on conventional FEM. However, structural element fractures can induce structural discontinuities, and increase the number of nodes and DoFs, which cannot be easily handled with conventional FEM approaches. Ting *et al*. [21, 22] and Shih *et al*. [23] proposed the vector form intrinsic finite element (VFIFE) method, based on Newton's second laws to model structural systems with mass particles. The underlying principle of the VFIFE method is the theory of vector mechanics [24]. In the VFIFE framework, a general description of particle motion is introduced to handle finite rigid body motion by incorporating an adaptive material frame in the basic definition for displacement and strain. The VFIFE method models the structure as a system of discrete mass particles, where the mass particle positions characterize the structure's shape and motion. Motion of each mass point satisfies Newton's second laws, and internal forces induced by deformation and the external load are applied at each mass point. Internal forces of the elements are calculated using the material reference frame and fictitious reversed rigid body motion. A simple central difference scheme is adopted to solve a set of equations of motion for particles. One major advantage of the VFIFE method is that it can process nonlinear or discontinuous issues without assembling a global stiffness matrix, avoiding problems of ill-conditioned matrixes. This shows great promise to simulate cracking, penetration, fragmentation, collision, and total collapse by separating or adding particles. The VFIFE method has been widely extended since it was proposed, and applied to nonlinear dynamic analysis and elasto-plastic analysis of truss [25, 26], frame [27, 28], membrane [29], and shell structures [30]. Yu *et al*. [31] simulated the progressive failure of truss structures and Duan *et al*. [32] analyzed the earthquake-induced collapse of cable-stayed bridge using VFIFE method. These studies [25-33] have verified the VFIFE method is efficient and powerful for simulation of structural behavior with large deformations and/or displacements. However, simulation of crack propagation by VFIFE method has not been reported previously.

This paper proposes a new strategy based on the VFIFE method to deal with crack propagation. Section 2 introduces the underlying concepts of VFIFE and describes cracking in the VFIFE framework. Section 3 details the proposed VFIFIE-*J*-integral method, combining the VFIFE and *J*-integral models, to simulate elastic cracking. The proposed method is validated for crack simulation of a notched plate under mode-I loading. Section 4 details the proposed VFIFE-FCM method, combining the FCM and VFIFE models, to simulate cohesive crack propagation. The proposed method is validated using crack propagation of a three point notched beam, comparing the resulting load deflection curves with literature results.

2. DESCRIPTION OF CRACK PROPAGATION IN FRAMEWORK OF VFIFE METHOD

The VFIFE method is a vector mechanics based computation method for solid media with large rotation and large deformation, and incorporates three fundamental concepts: point value description, path element, and fictitious reverse motion [24]. The primary objective of VFIFE is to handle motion and deformation of a system of multiple continuous bodies and their interactions [24]. Some VFIFE concepts and computation procedures are similar to conventional FEM analysis. However, in contrast to other formulations, the shape and position of a solid are described by mass particle motions. The mass particles are connected to the nodes of elements,

https://doi.org/10.1017/jmech.2017.85 Published online by Cambridge University Press

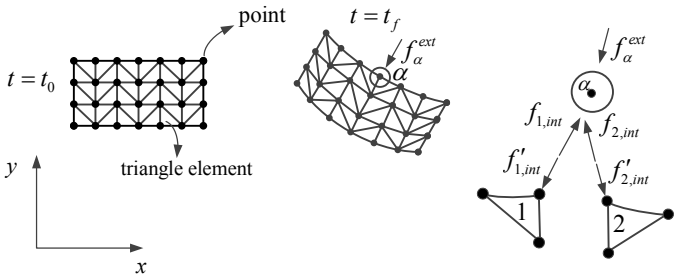


Fig. 1 Point value description for solid body.

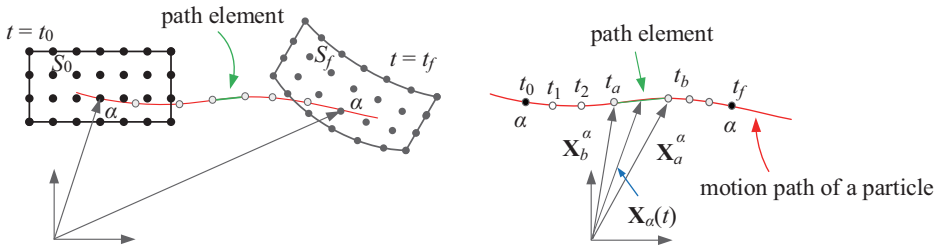


Fig. 2 A motion trajectory of an arbitrary particle α on a structure (a) A motion trajectory of a structure from $t = t_0$ to $t = t_f$ (b) the motion path of a particle α.

where the elements are massless, deformable, and of which the shape functions satisfy continuity requirements. Element nodal forces are obtained through the principle of virtual work. Internal force (reaction force to element nodal forces), external forces, and boundary conditions are imposed on the mass particles. Thus, the motion of each mass particle is governed by Newton's second law, rather than the differential equation of the conventional analytical method. Therefore, VFIFE assumes strong equilibrium at each mass particle, whereas conventional FEM assumes weak equilibrium. Consequently, the VFIFE method has no concept of global stiffness matrix, and avoids the problem of ill-conditioned matrices. An explicit solution procedure, e.g. the central difference method, is adopted to solve the governing equation. Particle motion in the current step is explicitly solved based on previous steps. We first introduce the underlying concepts of VFIFE theory: point value description, path element, and fictitious reverse motion, and then propose a description for crack propagation in the VFIFE framework.

2.1 Point Value Description

Figure 1 shows that a solid body can be described as many points linked by a set of triangular elements. The motion of the solid body is determined by the particles; i.e. the triangle elements are deformed according to the particle motions. The motion of each individual mass particle follows the Newton's second law. At time t, a particle α has mass m_α and displacement vector $\mathbf{d}_\alpha(t)$. The equation of motion for particle α is

$$\mathbf{m}_\alpha \ddot{\mathbf{d}}_\alpha = \mathbf{F}_\alpha^{ext} + \mathbf{F}_\alpha^{int} \tag{1}$$

where $\mathbf{F}_\alpha^{ext} = \sum f_{i,ext}$ is sum of external forces $f_{i,ext}$ acting on particle α, $\mathbf{F}_\alpha^{int} = \sum f_{i,int}$ is the sum of internal forces $f_{i,int}$ exerted on particle α by the elements connected to it. Note that $f'_{i,\text{int}}$ in Fig. 1 is the reacting force exerted on the element by the mass particle α.

2.2 Path Element

The trajectory segment is referred to as a path element if the particle motion is continuous and can be analytically expressed by the same equation within this time segment. Figure 2 shows a motion trajectory of an arbitrary particle α. The trajectory consists of a set of segments identified by a series of time instants t_i, $i = 0, 1, 2, \ldots, a, b, \ldots, f$. The displacement of α within a path element $t_a \le t \le t_b$ is donated by the continuous time function $x_\alpha(t)$, and the displacements of α in time t_a and t_b are $\mathbf{x}_a^\alpha$ and $\mathbf{x}_b^\alpha$, respectively. In the path element $t_a \le t \le t_b$, the particle motion is continuous and the deformation is small. However, discontinuous motion occurs between the neighboring path elements e.g. t_a or t_b.

2.3 Fictitious Reverse Motion

To calculate the internal forces, pure deformation of the element is essential. Fictitious reverse motion is used to obtain the pure deformation by deducting the

https://doi.org/10.1017/jmech.2017.85 Published online by Cambridge University Press

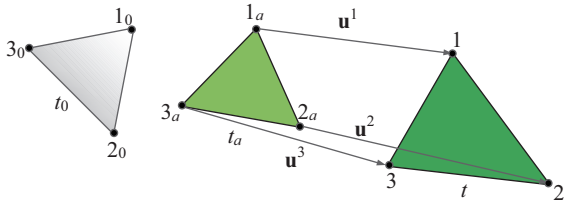


Fig. 3 The motion of a triangular element within an arbitrary path element $t_a \le t \le t_b$.

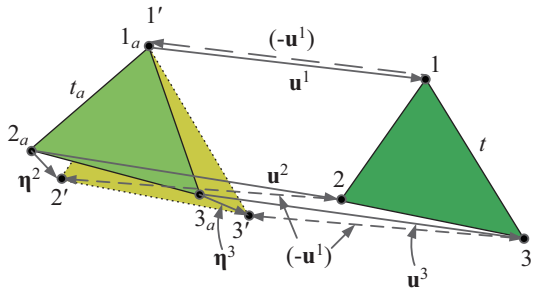


Fig. 4 Fictitious reverse rigid-body translation of a triangular element.

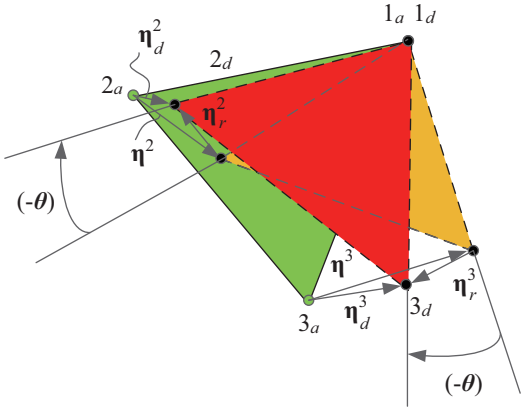


Fig. 5 Fictitious reverse rigid-body rotation of a triangular element.

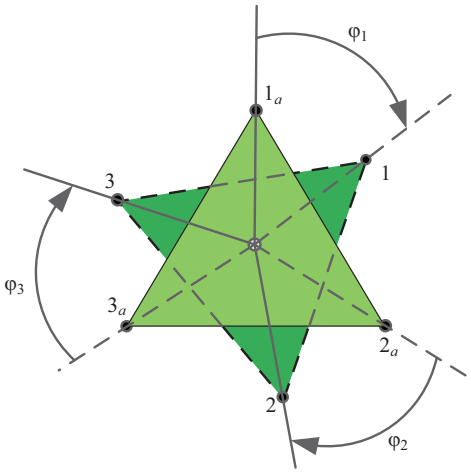


Fig. 6 The estimation of the rotational angle $(-\theta)$.

displacement caused by the rigid body translation and rotation from the total displacement. Therefore, fictitious reverse motion consists of fictitious reverse translation and fictitious reverse rotation. Figure 3 shows the motion of a triangular planar solid element with three particles within an arbitrary path element $t_a \le t \le t_b$. The planar element geometry is defined by three particles with node numbers (1, 2, 3) at time t and (1_a, 2_a, 3_a) at time t_a. The position vectors of node j (j = 1, 2, 3) at t_a and t are $\mathbf{x}_a^j$ and $\mathbf{x}^j$, respectively. From t_a to t, the increments of node translations are

$$\mathbf{u}^j = \mathbf{x}^j - \mathbf{x}_a^j \tag{2}$$

The triangular element at time t has undergone a rigid body motion, including rigid body translation and rigid body rotation. It is assumed that the displacement increments of node 1 are the rigid body translation of the element. For deducting the displacement caused by rigid body translation, a fictitious reverse rigid translation ($-\mathbf{u}^1$) of the triangular element is applied from t to t_a, as shown in Fig. 4, and the relative displacements are

$$\boldsymbol{\eta}^j = \mathbf{u}^j + \left(-\mathbf{u}^1\right), \quad j = 1,2,3 \tag{3}$$

Then the fictitious reverse rigid body rotation $(-\theta)$ is used to deduct the displacement caused by rigid body rotation, as shown in Fig. 5, and the nodal displacements due to the in-plane rigid body rotation displacement are

$$\boldsymbol{\eta}_r = \left[\mathbf{R}_r\left(-\theta\right) - \mathbf{I}\right]\left(\mathbf{x} - \mathbf{x}^1\right) \tag{4}$$

where $\mathbf{R}_r\left(-\theta\right) = \begin{bmatrix} \cos(-\theta) & \sin(-\theta) \\ -\sin(-\theta) & \cos(-\theta) \end{bmatrix}$ is the rotation matrix [22].

Pure deformation of the nodes, $\boldsymbol{\eta}_d^j$, can be expressed as

$$\boldsymbol{\eta}_d^j = \boldsymbol{\eta}^j + \boldsymbol{\eta}_r^j \tag{5}$$

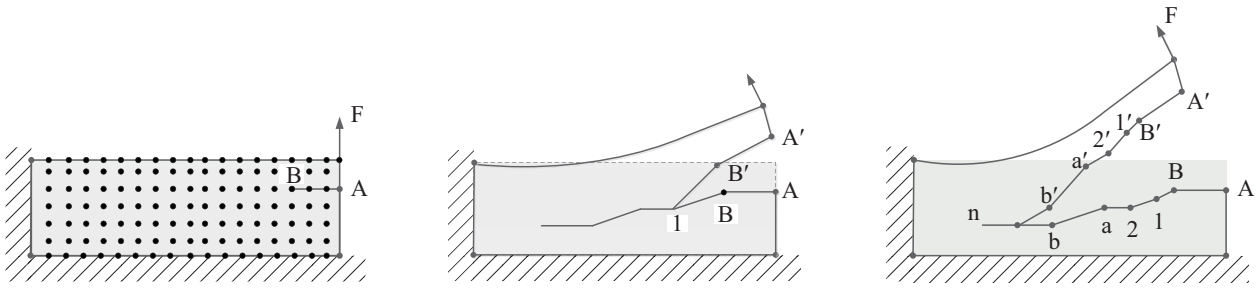
Let the centroid of the element at time t_a and t coincide, and the angle between the two lines connecting the element nodes and centroid be φ_j as shown in Fig. 6. Then the average rotation can be assumed to be

$$\theta = \frac{1}{3}\sum_{j=1}^{3}\varphi_j \tag{6}$$

2.4 Calculation of the Internal Force

The internal force can be calculated from the pure deformation using engineering strain and stress. Similar to traditional FEM, the nodal internal force at the fictitious state can be expressed as

https://doi.org/10.1017/jmech.2017.85 Published online by Cambridge University Press



(a) (b) (c)

Fig. 7 A plane structure with a notch A-B (a) The continuous body is described by a set of mass particles (b) The particle at the crack tip (B) separates into two new particles(B and B′) (c) crack propagation.

$$\hat{\mathbf{f}}_j = \begin{Bmatrix} \hat{f}_{jx} \\ \hat{f}_{jy} \end{Bmatrix} = \hat{\mathbf{f}}_{ja} + \Delta\hat{\mathbf{f}}_j \tag{7}$$

where $\hat{\mathbf{f}}_{ja}$ is the internal force at t_a and $\Delta\hat{\mathbf{f}}_j$ is the incremental internal force during $t - t_a$ from the principle of virtual work, the three components of incremental internal force can be expressed as

$$\Delta\hat{\mathbf{f}}_s = \left\{\Delta\hat{f}_{2x} \;\; \Delta\hat{f}_{3x} \;\; \Delta\hat{f}_{3y}\right\}^T = \int_{V_a} \hat{\mathbf{B}}^T \hat{E}_a \hat{\mathbf{B}} \Delta\mathbf{u}_s dV_a \tag{8}$$

and the other nodal internal forces can be obtained from the equilibrium condition

$$\begin{aligned} &\sum M_z = 0, \quad \Delta\hat{f}_{2y} = \frac{1}{\hat{x}_2}\left(\Delta\hat{f}_{2x}\hat{y}_2 + \Delta\hat{f}_{3x}\hat{y}_3 - \Delta\hat{f}_{3y}\hat{y}_3\right) \\ &\sum F_{\hat{x}} = 0, \quad \Delta\hat{f}_{1x} = -\left(\Delta\hat{f}_{2x} + \Delta\hat{f}_{3x}\right) \\ &\sum F_{\hat{y}} = 0, \quad \Delta\hat{f}_{1y} = -\left(\Delta\hat{f}_{2y} + \Delta\hat{f}_{3y}\right) \end{aligned} \tag{9}$$

In contrast to traditional FEM, the principle of virtual work and equilibrium condition are defined by increment. Thus, only three independent variables (u_2, u_3, v_3) are defined [24].

The real internal force at t can be obtained by the forward rotation

$$\mathbf{f}_j = \begin{Bmatrix} f_{jx} \\ f_{jy} \end{Bmatrix} = \begin{bmatrix} \mathbf{R}^{\mathrm{T}}\hat{\mathbf{Q}}^{\mathrm{T}} & \mathbf{0} \\ \mathbf{0} & 1 \end{bmatrix} \hat{\mathbf{f}}_j \tag{10}$$

where $\mathbf{R}$ is the defined rotation matrix, and $\mathbf{Q}$ is the rotation matrix between deformation and domain coordinates [24]. The reacting force ($\mathbf{f}'_j$) on the element is $-\mathbf{f}_j$.

After obtaining the internal force, the new particle position can be obtained from Eq. (1) using a center difference method. The trajectory of all particles can be solved following the sequence: new position → new internal force → next new position.

2.5 Description of Crack in VFIFE

Consider a planar structure with a notch that stretches gradually from B with the increased force F, as shown in Fig. 7. The continuous body is described by a set of mass particles (Fig. 7(a)), where the motion of each particle follows Newton's second law. A group of path elements are defined to describe the motion of the continuous body. Deformation of the particle in the path element is continuous, as discussed above, and cracking occurs at the instant between the neighboring path elements. Internal forces for each particle are calculated using fictitious reverse motion. The particle at the crack tip (B) separates into two new particles (B and B′) if cracking occurs (Fig. 7(b)), and particles B and B′ masses should be updated after the separation. Thus, crack propagation can be described by the separated mass particles A(A′)-B(B′)-…-b(b′)-n (Fig. 7(c)).

3. SIMLUATION OF ELASTIC CRACK PROPAGATION

Various techniques have been developed for crack evaluation in concrete structures, including quarter point displacement [34], *J*-integral [5], FCM [6], and two parameter fracture models [8]. This section introduces the VFIFE-*J*-integral method, combining VFIFE and *J*-integral methods, to calculate SIF at the crack tip.

3.1 VFIFE-*J*-Integral

Prior to describing the proposed method, we recall some basic concepts concerning asymptotic fields in fracture mechanics. The stress field near the crack tip for mode I is determined by r, θ and K_I, as shown in Fig. 8, where K_I is the SIF and reflects the stress singularity near the tip, and is commonly calculated using the *J*-integral method. The *J*-Integral provides a path-independent value for all paths surrounding a class of notches in two-dimensional deformation fields of linear or non-linear elastic materials [15]. SIF can be evaluated by *J*-Integral when yielding occurs on a small scale compared to the notch size. The VFIFE-*J*-integral method develops the *J*-integral method within the VFIFE framework.

3.1.1 Definition of *J*-Integral

Consider a homogeneous body of linear or non-linear elastic material, free of body forces and subjected to a two-dimensional deformation field. Suppose the body

https://doi.org/10.1017/jmech.2017.85 Published online by Cambridge University Press

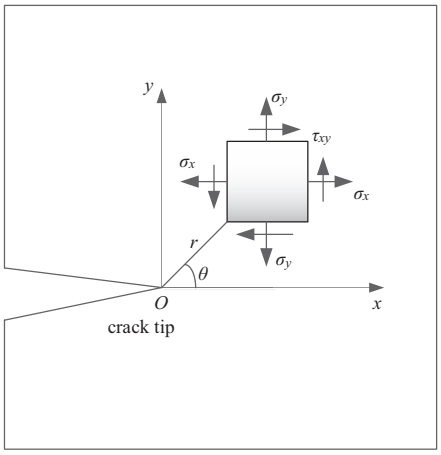


Fig. 8 Stress fields near the crack tip.

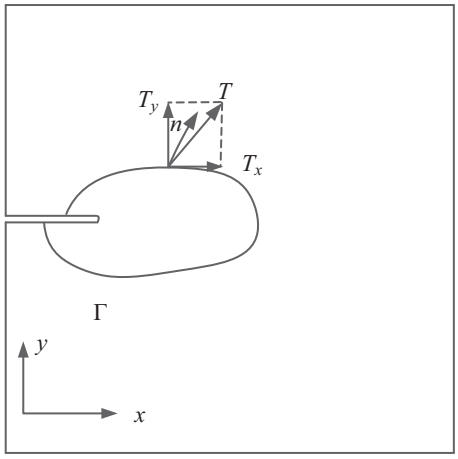


Fig. 9 An arbitrary integral curve surrounding the crack tip.

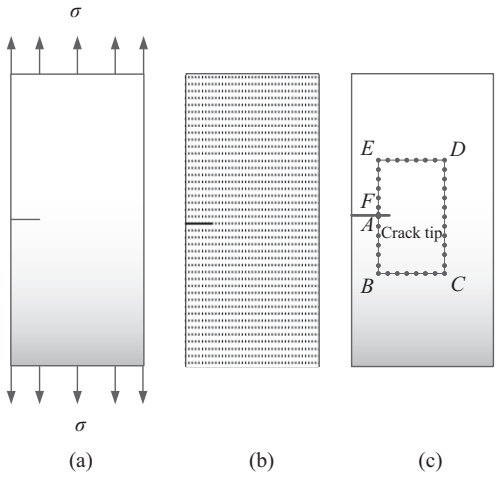


Fig. 10 A plate with a tensile edge crack (a) a tensile edge crack with flat surfaces parallel to the *x*-axis (b) mass particles modeling the plate (c) a integral path.

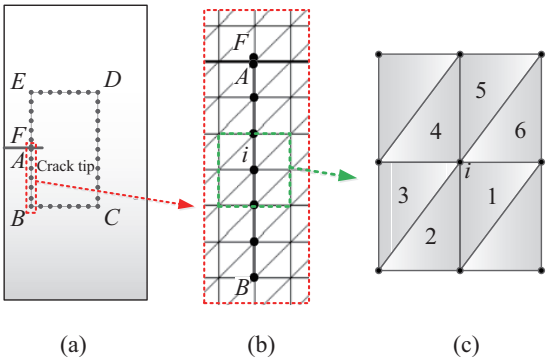


Fig. 11 The integral path and the element type (a) the integral path *ABCDEF* (b) the nodes on the path *AB* (c) the elements surrounding the particles.

contains a notch with a flat surface parallel to the *x*-axis, as shown in Fig. 9. Then the *J*-Integral can be expressed as [5]

$$J=\int_{\Gamma}\left[Wdy-\left(T_x\frac{\partial u_x}{\partial x}+T_y\frac{\partial u_y}{\partial x}\right)ds\right] \tag{11}$$

where $W=\int_0^{\varepsilon}\sigma_{ij}d\varepsilon_{ij}$ is the strain energy density; Γ is an arbitrary curve surrounding the crack tip; and T_x and T_y are the traction along the *x* and *y* axes, respectively,

$$T_x=\sigma_x n_x+\tau_{xy}n_y,\quad T_y=\sigma_y n_y+\tau_{xy}n_x \tag{12}$$

3.1.2 Numerical Implementation of the *J*-Integral by VFIFE Method

Consider a tensile edge crack with flat surface parallel to the *x*-axis that has an arbitrary path, as shown in Fig. 10. The *J*-integral from Eq. (11) is calculated along Γ starting from an arbitrary point on the flat part of the lower notch surface and terminating at an arbitrary point on the flat part of the upper notch surface. To facilitate the calculation, the path (*ABCDEF*) along the edge of element is selected, as shown in Fig. 10(c), and

$$J_{ABCDEF}=J_{AB}+J_{BC}+J_{CD}+J_{DE}+J_{EF} \tag{13}$$

and we estimate J_{ABCDEF} as

$$\begin{aligned}J&=\int_{\Gamma}\left[Wdy-\left(T_x\frac{\partial u_x}{\partial x}+T_y\frac{\partial u_y}{\partial x}\right)ds\right]\\&\cong\sum_{i=1}^{n-1}\left[\bar{W}_i\Delta y_i-\left(\bar{T}_x^i\frac{\partial\bar{u}_x^i}{\partial x}+\bar{T}_y^i\frac{\partial\bar{u}_y^i}{\partial x}\right)\Delta s_i\right]\end{aligned} \tag{14}$$

where *i* is the number of nodes on the integral path, *n* the total number of nodes on the integral path $\bar{W}_i=\frac{W_i+W_{i+1}}{2}$, $\Delta y_i=y_{i+1}-y_i$, and $\Delta s_i=s_{i+1}-s_i$. The *J*-integral can be

https://doi.org/10.1017/jmech.2017.85 Published online by Cambridge University Press

expressed as the sum of the two parts

$$J = J^{(1)} + J^{(2)}, \quad J^{(1)} = \sum_{i=1}^{n-1} \overline{W}_i \Delta y_i,$$

$$J^{(2)} = -\sum_{i=1}^{n-1} \left(\overline{T}_x^i \frac{\partial \overline{u}_x^i}{\partial x} + \overline{T}_y^i \frac{\partial \overline{u}_y^i}{\partial x} \right) \Delta s_i \tag{15}$$

Let us calculate $J^{(1)}$ on path AB as an example. The integral path AB is assumed along with several nodes and every node is surrounded by triangle elements, as shown in Fig. 11. For node i, the strain energy density is

$$W_i = \frac{\sum_{j=1}^{m} W_j A_j}{\sum_{j=1}^{m} A_j} \tag{16}$$

where $i = 1, 2, \ldots, n$, and W_j and A_j are the energy density and area of the jth element around node i, respectively.

From Eq. (15), the first part of the J-integral is

$$J^{(1)} = \sum_{i=1}^{n-1} \overline{W}_i \Delta y_i = \sum_{i=1}^{n-1} \frac{W_i + W_{i+1}}{2} (y_{i+1} - y_i) \tag{17}$$

and the stress of every node can be calculated from

$$\sigma_x^i = \frac{\sum_{j=1}^{m} \sigma_x^j A_j}{\sum_{j=1}^{m} A_j}, \quad \sigma_y^i = \frac{\sum_{j=1}^{m} \sigma_y^j A_j}{\sum_{j=1}^{m} A_j}, \quad \tau_{xy}^i = \frac{\sum_{j=1}^{m} \tau_{xy}^j A_j}{\sum_{j=1}^{m} A_j} \tag{18}$$

The average stress for every node is

$$\overline{\sigma}_x^i = \frac{\sigma_x^i + \sigma_x^{i+1}}{2}, \quad \overline{\sigma}_y^i = \frac{\sigma_y^i + \sigma_y^{i+1}}{2}, \quad \overline{\tau}_{xy}^i = \frac{\tau_{xy}^i + \tau_{xy}^{i+1}}{2} \tag{19}$$

and so, from Eq. (12), the traction of each node is

$$T_x^i = \overline{\sigma}_x^i n_x^i + \overline{\tau}_{xy}^i n_y^i, \quad T_y^i = \overline{\sigma}_y^i n_y^i + \overline{\tau}_{xy}^i n_x^i \tag{20}$$

To calculate the derivatives of the displacement vector, i.e., $\frac{\partial u_x}{\partial x}$ and $\frac{\partial u_y}{\partial x}$, the integral path is assumed to move a small distance, $\frac{\Delta x}{2}$, in the positive and negative x directions respectively. Then paths $\Gamma - \frac{\Delta x}{2}$ and $\Gamma + \frac{\Delta x}{2}$ can be obtained as shown in Fig. 12, and the derivatives of the displacement vector for each node, $\frac{\partial u_x^i}{\partial x}$ and $\frac{\partial u_y^i}{\partial x}$, are

$$\frac{\partial u_x^i}{\partial x} = \frac{\Delta u_2^i - \Delta u_1^i}{\Delta x}, \quad \frac{\partial u_y^i}{\partial x} = \frac{\Delta v_2^i - \Delta v_1^i}{\Delta x} \tag{21}$$

where Δu_1 and Δv_1 are displacements on path $\Gamma - \frac{\Delta x}{2}$,

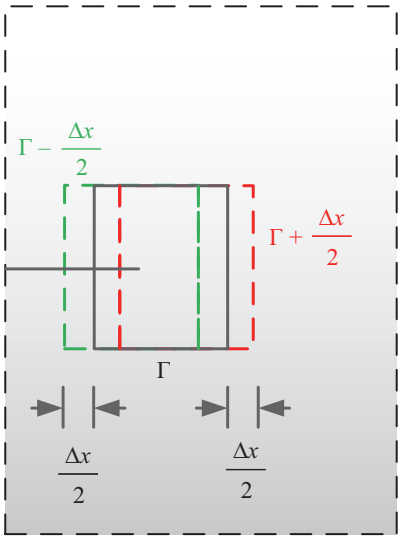


Fig. 12 Path shifts by a small distance $\frac{\Delta x}{2}$ in the positive and negative x-directions.

and Δu_2 and Δv_2 are displacements on path $\Gamma + \frac{\Delta x}{2}$. Thus, the average derivatives of the displacement vector of each node can be expressed as

$$\frac{\partial \overline{u}_x^i}{\partial x} = \frac{\frac{\partial u_x^i}{\partial x} + \frac{\partial u_x^{i+1}}{\partial x}}{2}, \quad \frac{\partial \overline{u}_y^i}{\partial x} = \frac{\frac{\partial u_y^i}{\partial x} + \frac{\partial u_y^{i+1}}{\partial x}}{2} \tag{22}$$

and the second part of the J-integral can be calculated from Eqs. (17-22).

By definition, the J-integral is always equal to the elastic strain energy release rate, G_I [35]. For model-I crack, the relationship between the elastic strain energy release rate and SIF is defined as

$$J = G_I = \begin{cases} \dfrac{K_I^2}{E} & \text{(plan stress)} \\ \dfrac{(1-\upsilon^2)K_I^2}{E} & \text{(plan strain)} \end{cases} \tag{23}$$

Thus, we can calculate the SIF according to Eq. (23). When the crack length is determined, the SIF increases with increasing loading force. The crack begins to propagate once the stress on the crack tip attains the critical value of material. The SIF at the critical stress field called critical SIF which is the fracture toughness K_c. Therefore, the crack behavior criteria for model-I loading is

$$K_I = K_{Ic} \tag{24}$$

3.2 A Plate with Tensile Edge Crack under Mode-I Loading

Figure 13 shows a plate with an edge crack. Tension is loaded with planar stress conditions, and the geometric

https://doi.org/10.1017/jmech.2017.85 Published online by Cambridge University Press

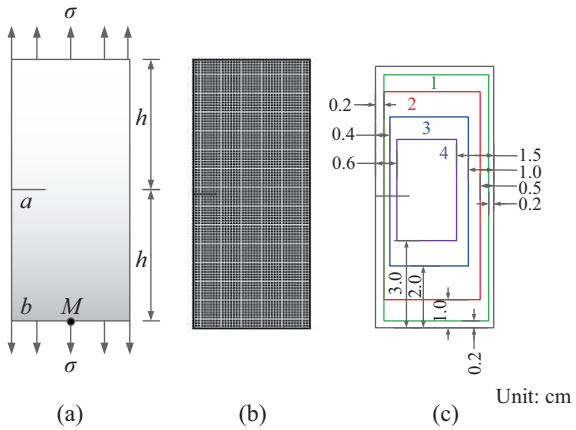


Fig. 13 (a) The rectangular plate with a tensile edge crack (b) mass particles modeling the plate (c) Three different integral paths.

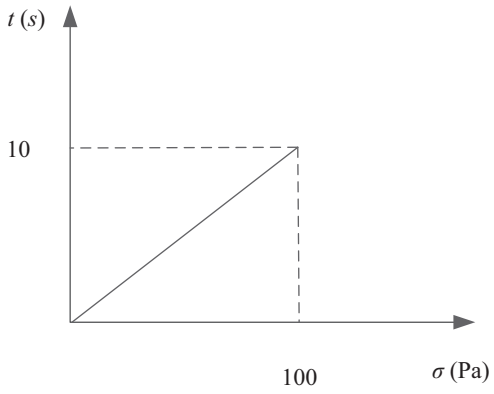


Fig. 14 The loading way.

Table 1 The K_I (Pa·m$^{1/2}$) values of the difference integral paths.

Integral path	K_I (J-integral)	K_I (FGC)	Errors
1	21.00	21.72	3.31%
2	20.99		3.36%
3	20.76		4.41%
4	20.73		4.56%

Table 2 The K_I values of the difference mesh numbers.

mesh	K_I (J-integral)	K_I (Duarte)	Errors
20 × 40	4.507	5.01	10.0%
40 × 80	4.847		3.25%
50 × 100	4.959		1.03%

parameters are chosen as a = 0.8 cm, b = 4 cm, h = 5 cm, elastic modulus E = 2 MPa, Poisson's ratio ν = 0.3, and loading force σ = 100 Pa, and the number of elements is 40 × 100 (Fig. 13(b)). M is the node at the bottom of the plate. The loading way is the ramp load and loading time = 10s, as shown in Fig. 14. The time step is h = 1.0 × 10^{-5} s. Four different paths (Fig. 13(c)) are selected to calculate the J-integral.

The SIF calculated by the proposed method is compared with a finite geometry corrected (FGC) model [2]

$$K_I=F\sigma\sqrt{\pi a} \tag{25}$$

where

$$F=1.12-0.231\left(\frac{a}{b}\right)+10.55\left(\frac{a}{b}\right)^2-21.72\left(\frac{a}{b}\right)^3 +30.39\left(\frac{a}{b}\right)^4 \tag{26}$$

Table 1 shows good agreement between the proposed and FGC values. Thus, the proposed method to calculate SIF by J-integral is correct and effective. In principle, the J-integral is path independent. However, in practice the error increases (3.31%, 3.36%, 4.41%, 4.56% respectively) for paths 1–4. Therefore, the integral path should be selected as far from the crack tip as possible when calculating SIF using the J-integral.

For comparing with the results of partition of unity (PU) method by Fan *et al*. [36], the geometric parameters in Fig. 13 are a = 1, b = 2, h = 2, elastic modulus E = 1, Poisson's ratio ν = 0.3, and loading force σ = 1. The same problem was previously solved by Duarte [37], and his results (K_I = 5.01) was used as benchmark in the reference of Fan *et al*. [36]. In the results of Fan *et al*. [36], when the orders of the polynomial-typed influence functions [36] for element are 2, 3, 4, and 5, the corresponding SIF values are 2.595, 4.528, 5.045, and 4.996, respectively. By using the present method, the predicted values of SIF with different mesh number are presented in Table 2 and yield good agreement with the benchmark value. In Table 2, the error decreases with the increasing of mesh number. When the mesh number is 50 × 100, the result (4.959) is very close to the best SIF value (4.996) by the PU method [36]. It is verified

https://doi.org/10.1017/jmech.2017.85 Published online by Cambridge University Press

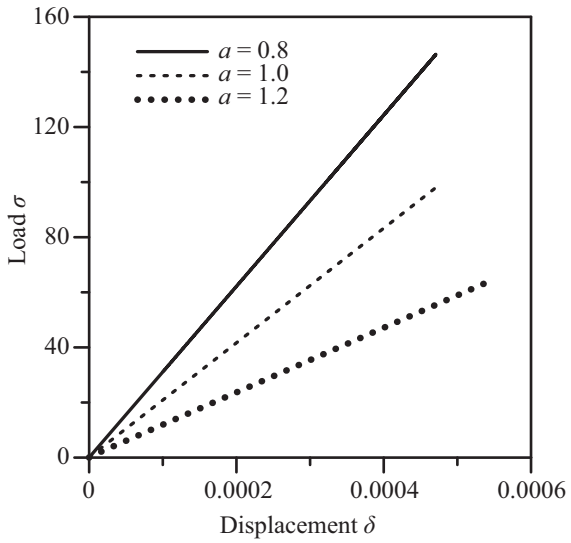


Fig. 15 The load-displacement curve of the node *M*.

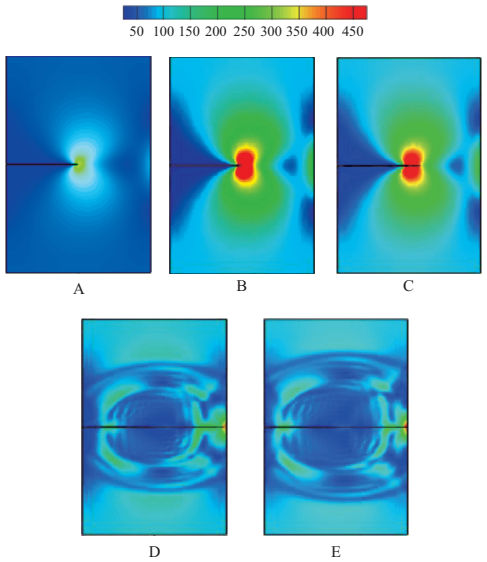


Fig. 16 The stress distribution of the plate.

that the present method is accurate for evaluating the SIF. The result is close to the exact solution when the mesh near the crack tip is dense. However, the calculation efficiency will be decreased when the mesh is dense.

Next, the crack propagation in linear elastic condition is simulated. Assuming the fracture toughness is K_{IC} = 483. The fracture criterion in Eq. (12) is used in this case. The load-displacement of the node *M* (Fig. 13) with different initial crack length is plotted in Fig. 15. As can be seen, the load-displacement curve is linear in this condition. When the initial crack lengths are 0.8, 1.0 and 1.2, the maximum loading force ($\sigma_{\max}$) obtained by the present method are 146.3, 98.61 and 63.77. Those results are very close to the analytical results (144.88, 96.44, and 61.80) calculated by Eq. (24). In Fig. 15, the maximum loading force becomes smaller when the initial crack length increases. The stress distributions of the plate and the shapes of crack at different stages are shown in Fig. 16. As the loading force increases, the stress near the crack tip becomes larger. When the SIF at the crack tip attains fracture toughness K_{IC}, the crack is beginning to propagate. The stress at crack tip is always larger than other place of the plate until the plate splits into two parts.

4. SIMULATION OF COHESIVE CRACK PROPAGATION

This section proposes VFIFE-FCM to simulate cohesive crack propagation. The FCM incorporating the assumption that cohesive force acts on the fracture process zone is integrated into the VFIFE framework.

4.1 The Fictitious Crack Model (FCM)

The FCM characterizes the tension softening fracture process zone through a fictitious crack ahead of the existing crack [6]. Figure 17 shows that the closing stress in the FPZ increases from zero at the tip of the existing traction free macro-crack to the full uniaxial tensile strength of the material, f_t, at the tip of the fictitious crack. The zone far from the crack remains elastic. Therefore, the stress-strain curve is linear, and the distribution of closing stress $\sigma(w)$ along the FPZ depends on the opening of the fictitious crack face, w.

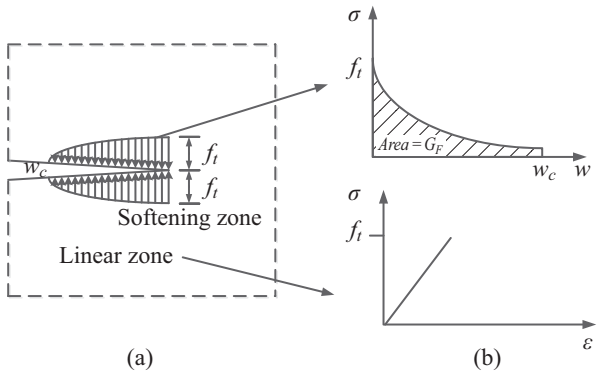


Fig. 17 (a) Fictitious crack model (b) Distribution of the stress in linear zone and softening zone.

In the FCM, the area under the tension softening curve is the true fracture energy,

$$G_F = \int_0^{f_t} w(\sigma)d\sigma = \int_0^{w_c} \sigma(w)dw \tag{27}$$

where f_t is the uniaxial tensile strength limit of material, and w_c is the critical tip opening displacement of the existing macro-crack.

In principle, the complete fracture process of a structure can be described once the two independent material parameters f_t and G_F are obtained, and the shape of the tension softening diagram will have considerable influence on G_F. In practice, it is common to make linear,

https://doi.org/10.1017/jmech.2017.85 Published online by Cambridge University Press

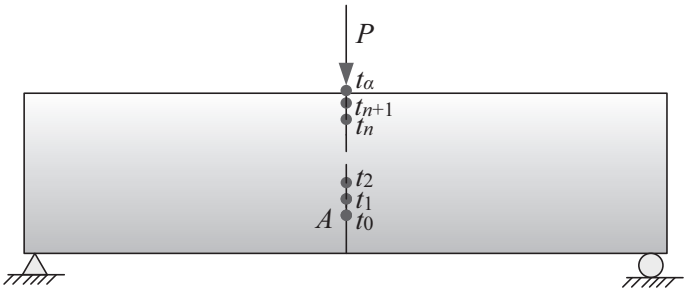


Fig. 18 The crack propagation process over the period of time $t_0 \le t \le t_\alpha$.

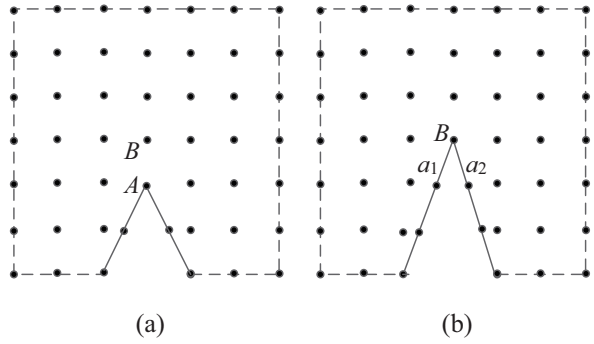


Fig. 19 The propagation process of crack tip. (a) before the cracking at node *A*. (b) after the cracking at node *A*.

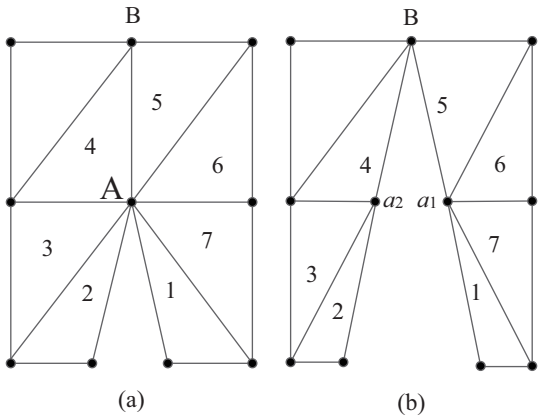


Fig. 20 Elements surrounding the particles (a) before the cracking at node A (b) after the cracking at node A.

bilinear, polynomial, and exponential approximations to $\sigma(w)$.

4.2 VFIFE- FCM Method

Figure 18 illustrates the proposed VFIFE-FCM for a three-point bending beam with a fracture zone. The fracture zone can be expected to follow a vertical line at the center of the element boundaries which are situated along this line. Cracking only occurs at the starting point of a VFIFE path element. It is assumed that the crack propagates over $t_0 \le t \le t_\alpha$, with the initial crack beginning at t_0. Before the loading force is exerted, there is a notch in the middle bottom of the beam, and *A* is the crack tip, as shown in Fig. 19(a). The tensile stress of the tip, σ_x^A, can be calculated at each time step as the loading force increases, and the cracking criterion is

$$\sigma_x^A \ge f_t \tag{28}$$

The material behaves elastically until stress reaches f_t. Once the tensile stress of the tip exceeds f_t at t_0, node *A* at the crack tip separates into two nodes, a_1 and a_2, and the crack tip propagates to node *B*, as shown in Fig. 19(b). The equations of motion of the particles after splitting are

$$\begin{aligned} &\bar{m}^s \left(\frac{d^2 \mathbf{x}^s}{dt^2} \right)_n = \mathbf{f}_t^s, \qquad n \ge n_0 \\ &\left(\frac{d\mathbf{x}^s}{dt} \right)_{n_0} = \dot{\mathbf{x}}^s (t_0), \qquad \left(\mathbf{x}^s \right)_{n_0} = \mathbf{x}^s (t_0) \end{aligned} \tag{29}$$

where $\bar{m}^s$, $s = a_1, a_2$ is the mass of the new particles, and n is the calculation step index. At t_0, $n = n_0$, and the mass of the new points are

$$\bar{m}^{a_1} = \bar{m}^{a_2} = \frac{m^A}{2} \tag{30}$$

The internal force on particle *A* (node *A*) is assembled by the elements surrounding it before cracking (Fig. 20(*a*)). After particle *A* splits into a_1 and a_2, the connectivity among elements and nodes is altered, and accordingly, the internal force on particle a_1 (or a_2) is assembled from the elements connected with the new particle, as shown in Fig. 20(b).

When the tensile force reaches f_t, the material near the crack tip behaves nonlinearly since node *A* at the crack tip separates into two nodes. Simultaneously, closing stress $\sigma(w)$ acts on the new interfaces (Fig. 21(b)), and decreases as the opening displacement increases. Particle parameters are updated and particles displacements calculated for the next step using the VFIFE method. This procedure is repeated until failure occurs. Figure 22 shows the flowchart for VFIFE cohesive crack growth simulation.

4.3 Three-Point Bending Beam

We consider two examples of three-point bending beams and simulate cohesive crack propagation using the proposed VFIFE-FCM method. First, we simulated a

https://doi.org/10.1017/jmech.2017.85 Published online by Cambridge University Press

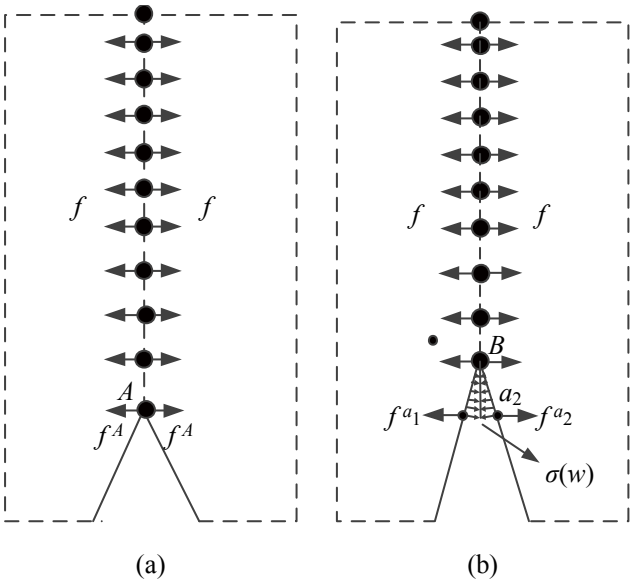


Fig. 21 The internal force and the cohesive force acting on the node in the process of cracking (a) before the node A cracking (b) after the node A cracking.

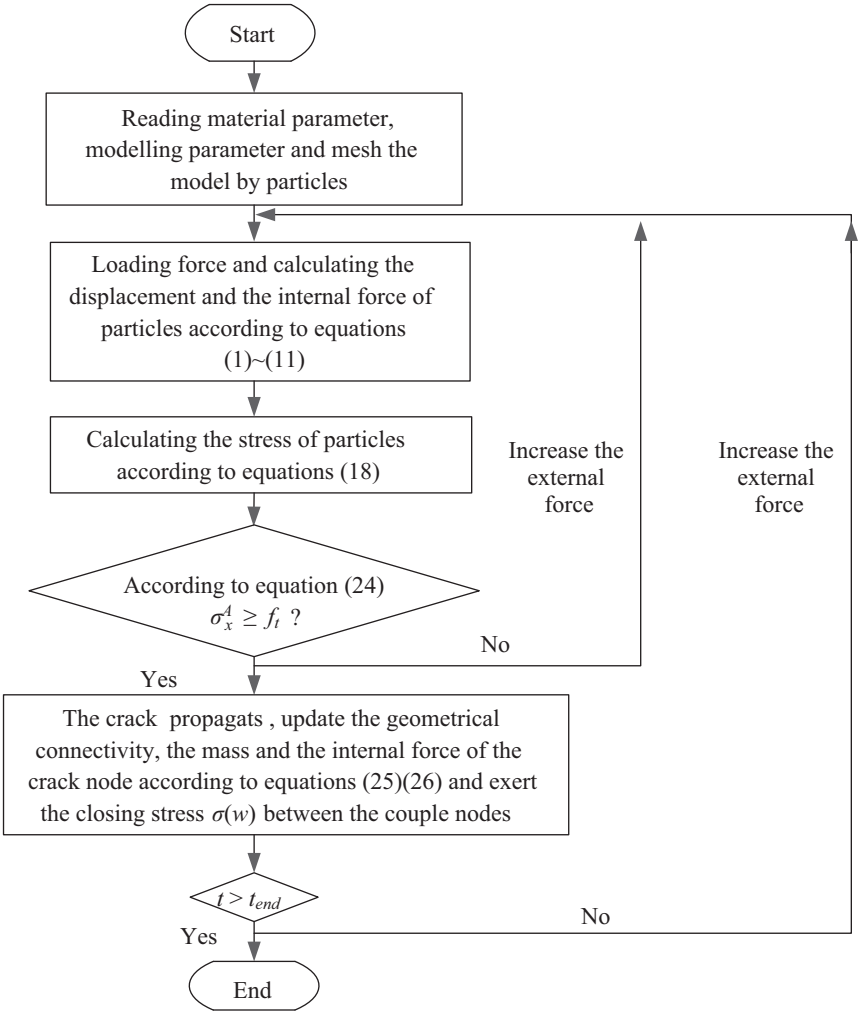


Fig. 22 A flowchart of the cohesive crack growth simulation.

https://doi.org/10.1017/jmech.2017.85 Published online by Cambridge University Press

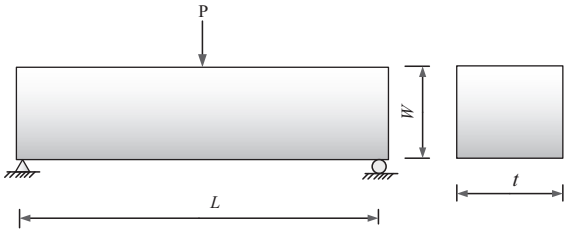


Fig. 23 A three-point bending beam.

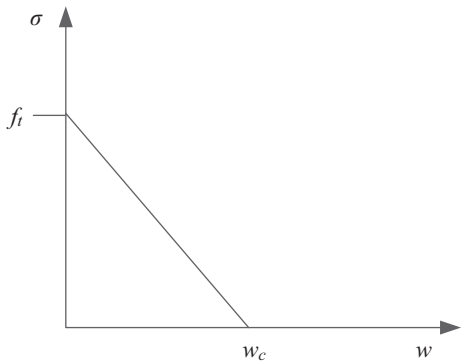


Fig. 24 The linear softening curve.

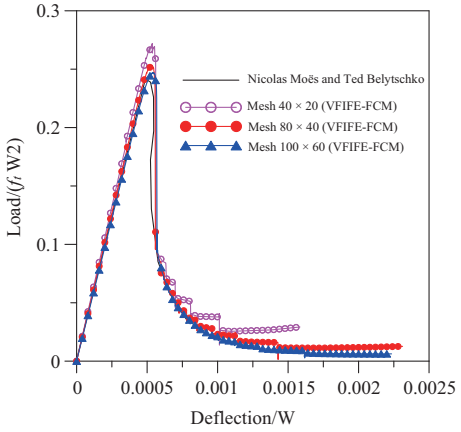


Fig. 25 Non-dimensional load-deflection curves for three-point bending beam.

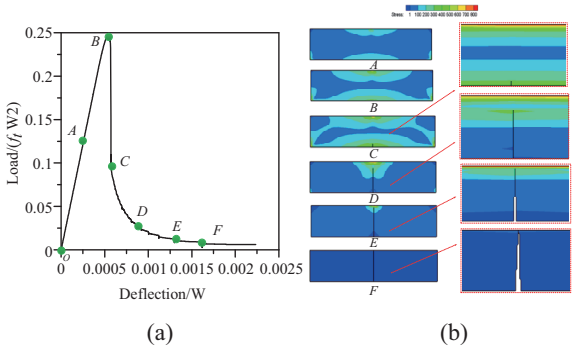


Fig. 26 The process of the cracking (a) non-dimensional load-deflection curve of mesh 100 × 60 (b) the stress distribution at different steps.

three-point beam without an initial notch and compared the VFIFE-FCM calculated load-displacement curve with that obtained by X-FEM. Second, we simulated VFIFE-FCM crack propagation for a three-point beam with an initial notch, and compared the outcomes with example results. The effects of different loading rates are also discussed.

4.3.1 Three-Point Bending Beam without Initial Notch

The example in Fig. 23 is propagation of a cohesive crack for a three-point bending beam without notch, which has been studied previously using X-FEM [18]. The geometrical parameters were $W = 0.15$ m, $L = 4\ W$, $t = W$, elastic modulus of the concrete $E = 36{,}500$ Mpa, ultimate tension stress $f_t = 3.19$ MPa, Poisson's ratio $v = 0.1$, and fracture energy $G_F = 50$ Nm^{-1}. The cohesive profile was linear, as shown in Fig. 24. Note that there was initially no crack in the beam. As the loading force increases, the cohesive zone starts to develop at the bottom midpoint of the beam when stress reaches f_t.

Figure 25 shows the load-deflection curves from VFIFE-FCM. Three different elements sets were considered: 40 × 20, 80 × 40, and 100 × 60. The results converged with increasing of element number. Results from the proposed method are close to those from Moës and Belytschko [18]. The load-deflection curve is linear before the crack appears. Then the slop of the curve begins to decrease as the crack emerges. The descending branch tends to flatten as the crack propagates. The computation time of the present method depends on the element number. However, as the present method do not need to assemblage the global stiffness matrix, the procedure of solving global matrix and iterative procedure are skipped. By this way, the computational efficiency is improved.

Figure 26 shows the cracking process. From the process *O*-*A*-*B*, the loading force increases linearly with increasing deflection until stress reaches f_t at point *B*. For the process *B*-*C*-*D*-*E*-*F*, the crack develops from the bottom to the top side, until total fracture of the beam at *F*. Stress distribution at different steps (*A* to *F*) and crack shapes at various stages of propagation are shown in Fig. 26(b). The beam splits into two parts when the crack propagates throughout the whole beam.

4.3.2 Three-Point Bending Notched Beam

Consider a three node bending beam with a notch in the middle bottom, as shown in Fig. 27. The geometric parameters were $W = 0.2$ m, $L = 4\ W$, $t = 0.08$ m, $a_0 = 0.3\ W$; the number of elements was 80 × 40; elastic modulus of concrete $E = 24.62$ GPa, ultimate compressive stress $f_c = 26.8$ MPa, ultimate tension stress $f_t = 2.58$

https://doi.org/10.1017/jmech.2017.85 Published online by Cambridge University Press

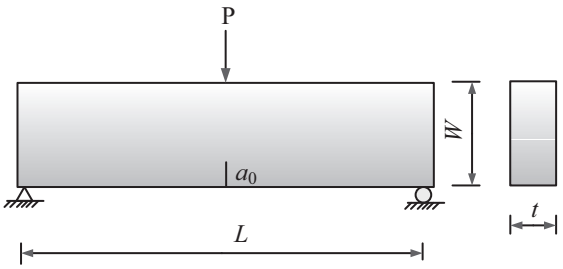


Fig. 27 Three-point bending notched beam.

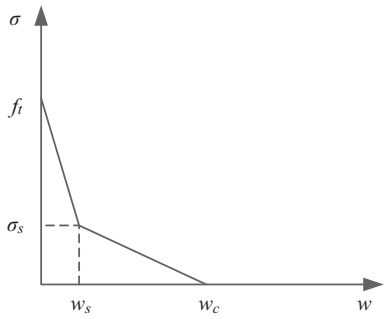


Fig. 28 The bilinear soften curve.

Table 3 The value of the coefficient α_F.

d_{max} (mm)	8	16	32
α_F	8	7	5

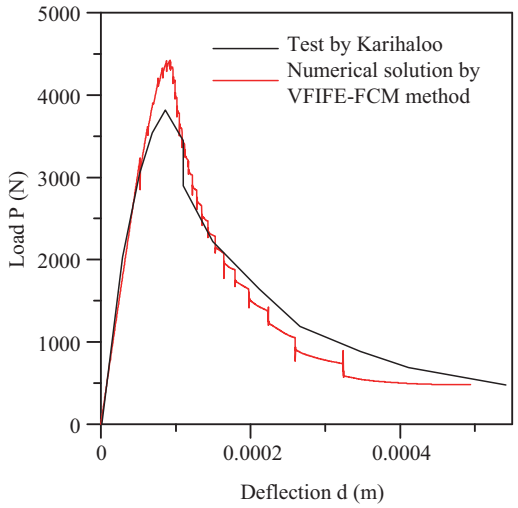


Fig. 29 The load-deflection curve of a three-point beading specimen.

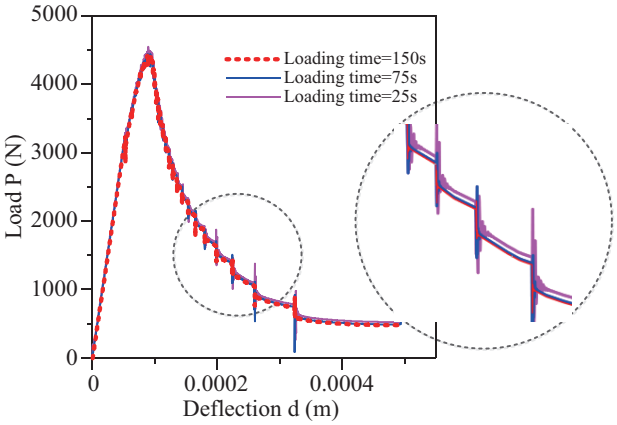


Fig. 30 The load-deflection curves at three different loading times.

Mpa, and Poisson's ratio $v = 0.1$. Displacement loading was used in this example, with total loading displacement = 0.5×10^{-3} m and loading time = 150 s. Fracture energy is [38]

$$G_F = \left(0.0204 + 0.0053 d_{\max}^{0.95}/8\right)\left(f_c / f_{c0}\right)^{0.7} \tag{31}$$

where f_{c0} = 10 MPa, d_{max} = 20 mm is the maximum size of the aggregate. Thus, $G_F = 63.42$ N/m^2.

The tension softening curve adopted in this example was recommended in the CEB-FIP Model Code 1990 standard [38], as shown in Fig. 28, and the bilinear tension softening function were

$$\begin{cases} \sigma = f_t\left(1 - 0.85\dfrac{w}{w_s}\right) & 0 \le w \le w_s \\ \sigma = 0.15 f_t \dfrac{w_c - w}{w_c - w_s} & w_s \le w \le w_c \\ \sigma = 0 & w \ge w_c \end{cases} \tag{32}$$

From the bilinear tension softening function, there are three parameters for the bilinear softening curve, where f_t is the ultimate tensile stress, and the other two parameters are [38]

$$\begin{cases} w_s = 2\dfrac{G_F}{f_t} - 0.15 w_c \\ w_c = \alpha_F \dfrac{G_F}{f_t} \end{cases} \tag{33}$$

where α_F is the coefficient that depends on the maximum aggregate size, shown in Table 3, and can be obtained by interpolation.

Figure 29 shows the load-deflection curve for a three point bending concrete specimen obtained by the proposed method compared with test data from Karihaloo [39]. The proposed method shows good agreement with the real test results, although the peak load of the numerical analysis is a little overestimated. This overestimation can be attributed to several reasons. First,

https://doi.org/10.1017/jmech.2017.85 Published online by Cambridge University Press

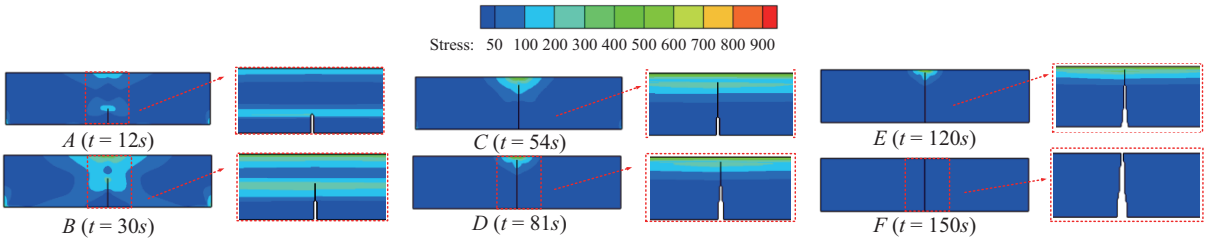


Fig. 31 The stress distribution over time.

the bilinear tension softening diagram may not reflect the real response well. Second, G_F as calculated from the estimate equation may be an overestimate. To some extent, G_F depends on the size of the structure member as well as other material properties not considered in the estimate equation.

To investigate the effect of loading rate on crack propagation, three different loading times were considered: 150, 75, and 25 s, as shown in Fig. 30. Loading rate has little influence on the load-deflection curve. Before crack propagation, the load-deflection is linear, then when the crack begins to propagate, the slop of the curve begins to decrease, with a slight oscillation as the crack propagates. The detailed softening response indicates that the curve oscillation tends to increase with increasing loading rate.

Figure 31 shows the crack length time deflection curve for 150 s loading time. Stress distributions at different instants (*A*, *B*, *C*, *D*, *E*, and *F*) of the cracking process are shown. Stress near the crack tip is always very large until the beam cracks completely. The fictitious crack appears when the stress at the tip reaches and exceeds the ultimate tensile stress, and then the cohesive force adds to the fictitious crack. The cohesive force becomes smaller with growth of the fictitious crack opening displacement. As the crack propagates, the beam splits into two parts eventually. Crack shapes at different instants are shown in Fig. 31.

5. CONLUSIONS

This paper proposes a new approach to simulate the cracking process in an efficient and reliable manner, without needing to consider the global stiffness matrix or artificially softening elements. A VFIFE-*J*-integral method is proposed to simulate elastic crack propagation under mode-I loading, and a VFIFE-FCM method to simulate cohesive crack propagation. For the VFIFE-*J*-integral method, the *J*-integral calculation method was developed within the VFIFE framework, and the calculated stress intensity at the crack tip was found to agree well with the finite geometry corrected value. Thus, the effectiveness of the proposed VFIFE-*J*-integral method was validated. For the VFIFE-FCM method, the fictitious crack model was integrated with the VFIFE framework to solve cohesive crack propagation. The computing procedure for the VFIFE-FCM method was developed in detail. The crack process of the three-point bending beam without notch was simulated, and the obtained load-deflection curve compared with that from X-FEM. The outcomes verified the accuracy of the proposed VFIFE-FCM method. Crack simulation of a three-point bending beam with a notch was also conducted and compared with the test result. The outcomes showed good agreement. The crack propagates very quickly once initiated from the notch tip. Crack propagation for three different loading rates was investigated and the results indicate that loading rate has little effect on the load-deflection curve in the linear stage before crack initiation, but oscillation of the curve in the softening stage tends to increase with increasing loading rate. Thus, the proposed VFIFE approach was validated as efficient and effective for simulation of crack propagation under mode-I loading. Further studies on crack propagation simulation under mode-II or mixed loadings and dynamic crack propagation are in progress and will be reported in the future.

ACKNOWLEDGEMENTS

This work is supported by National Natural Science Foundation of China (51522811, 51478429, and 90915008), Zhejiang Provincial Natural Science Foundation of China (LR13E080001), and the Fundamental Research Funds for the Central Universities (2015XZZX004-28).

REFERENCES

1. Griffith, A. A., "The Phenomena of Rupture and Flow in Solids," *Philosophical Transactions of the Royal Society of London*, **A221**, pp. 163-198 (1920).
2. Ewalds, H. and Wanhill, R., *Fracture Mechanics*, Edward Arnold, New York (1989).
3. Irwin, G. R., "Analysis of Stresses and Strains Near the End of a Crack Traversing a Plate," *Journal of Applied Mechanics*, **24**, pp. 361-364 (1957).
4. Bažant, Z. P. and Planas, J., *Fracture and Size Effect in Concrete and Other Quasi-Brittle Materials*, CRC Press, Boca Raton (1998).
5. Moës, N. and Belytschko, T., "Extended Finite Element Method for Cohesive Crack Growth," *Engineering Fracture Mechanics*, **69**, pp. 813-833

https://doi.org/10.1017/jmech.2017.85 Published online by Cambridge University Press

(2002).

6. Hillerborg, A., Modéer, M. and Petersson, P. E., "Analysis of Crack Formation and Crack Growth in Concrete by Means of Fracture Mechanics and Finite Elements," *Cement and Concrete Research*, **6**, pp. 773-782 (1976).
7. Hillerborg, A., "The Theoretical Basis of a Method to Determine the Fracture Energy G_F of Concrete," *Material and Structures*, **18**, pp. 291-296 (1985).
8. Xu, S. L. and Rrinhardt, H. W., "Determination of Double-*K* Criterion for Crack Propagation in Quasi-Brittle Fracture, Part I: Experimental Investigation of Crack Propagation," *International Journal of Fracture*, **98**, pp. 111-149 (1999).
9. Karihaloo, B. L., *Fracture Mechanics and Structural Concrete*, Longman Scientific & Technical, New York, pp. 1-45 (1995).
10. Belytschko, T., Fish, J. and Engelmann, B. E., "A Finite Element with Embedded Localization Zones," *Computer Methods in Applied Mechanics and Engineering*, **70**, pp. 59-89 (1988).
11. Zhuang, Z. and O'donoghue, P. E., "The Recent Development of Analysis Methodology for Rapid Crack Propagation and Arrest in Gas Pipelines," *International Journal of fracture*, **101**, pp. 269-290 (2000).
12. Miehe, C. and Gürses, E., "A Robust Algorithm for Configurational-Force-Driven Brittle Crack Propagation with R-Adaptive Mesh Alignment," *International Journal for Numerical Methods in Engineering*, **72**, pp. 127-155 (2007).
13. Blandford, G. E., Ingraffea, A. R. and Liggett, J. A., "Two-Dimensional Stress Intensity Factor Computations Using the Boundary Element Method," *International Journal for Numerical Methods in Engineering*, **17**, pp. 387-404 (1981).
14. Belytschko, T. and Tabbara, M., "Dynamic Fracture Using Element-Free Galerkin Methods," *International Journal for Numerical Methods in Engineering*, **39**, pp. 923-938 (1996).
15. Mellenk, J. M. and Babuška, I., "The Partition of Unity Finite Element Method: Basic Theory and Application," *Computer Methods in Applied Mechanics and Engineering*, **139**, pp. 289-314 (1996).
16. Babuška, I. and Melenk, J. M., "The Partition of Unity Method," *International Journal for Numerical Methods in Engineering*, **40**, pp. 727-758 (1997).
17. Babuška, I., Banerjee, U. and Osborn, J. E., "Generalized Finite Element Methods: Main Ideas, Results, and Perspective," *International Journal of Computational Methods*, **1**, pp. 67-103 (2004).
18. Moës, N. and Belytschko, T., "Extended Finite Element Method for Cohesive Crack Growth," *Engineering Fracture Mechanics*, **69**, pp. 813-833 (2002).
19. Song, J. H., Areias, P. M. A. and Belytschko, T., "A Method for Dynamic Crack and Shear Band Propagation with Phantom Nodes," *International Journal for Numerical Methods in Engineering*, **67**, pp. 868-893 (2006).
20. Liu, W., Yang, Q. D., Mohammadizadeh, S. and Su, X. Y., "An Efficient Augmented Finite Element Method for Arbitrary Cracking and Crack Interaction in Solids," *International Journal for Numerical Methods in Engineering*, **99**, pp. 438-468 (2014).
21. Ting, E. C., Shih, C. and Wang, Y. K., "Fundamentals of a Vector Form Intrinsic Finite Element: Part I. Basic Procedure and a Plane Frame," *Journal of Mechanics*, **20**, pp. 113-122 (2004).
22. Ting, E. C., Shih, C. and Wang, Y. K., "Fundamentals of a Vector Form Intrinsic Finite Element: Part II. Plane Solid Elements," *Journal of Mechanics*, **20**, pp. 123-132 (2004).
23. Shih, C., Wang, Y. K. and Ting, E. C., "Fundamentals of a Vector Form Intrinsic Finite Element: Part III. Convected Material Frame and Examples," *Journal of Mechanics*, **20**, pp. 133-143 (2004).
24. Ting, E. C., Duan, Y. F. and Wu, T. Y., *Vector Mechanics of Structure*, Science Press, BeiJing (2012).
25. Wang, C. Y., Wang, R. Z., Chuang, C. C. and Wu, T. Y., "Nonlinear Dynamic Analysis of Reticulated Space Truss Structures," *Journal of Mechanics*, **22**, pp. 199-212 (2006).
26. Xu, R., Li, D. X., Jiang, J. P. and Liu, W., "Adaptive Fuzzy Vibration Control of Smart Structure with VFIFE Modeling," *Journal of Mechanics*, **31**, pp. 671-682 (2015).
27. Wu, T. Y., Wang, R. Z. and Wang, C. Y., "Large Deflection Analysis of Flexible Planar Frames," *Journal of the Chinese Institute of Engineers*, **29**, pp. 593-606 (2006).
28. Wang, R. Z., Tsai, K. C. and Lin, B. Z., "Extremely Large Displacement Dynamic Analysis of Elastic–Plastic Plane Frames," *Earthquake Engineering and Structural Dynamics*, **40**, pp. 1515-1533 (2011).
29. Wu, T. Y. and Ting, E. C., "Large Deflection Analysis of 3D Membrane Structures by a 4-Node Quadrilateral Intrinsic Element," *Thin-Walled Structures*, **46**, pp. 261-275 (2008).
30. Wu, T. Y., "Dynamic Nonlinear Analysis of Shell Structures Using a Vector Form Intrinsic Finite Element," *Engineering Structures*, **56**, pp. 2028-2040 (2013).
31. Yu, Y., Paulino, G. H. and Luo, Y., "Finite Particle Method for Progressive Failure Simulation of Truss Structures," *Journal of Structural Engineering ASCE*, **137**, pp. 1168-1181 (2011).
32. Duan, Y. F. *et al*., "Entire-Process Simulation of Earthquake-Induced Collapse of a Mockup Cable-Stayed Bridge by Vector Form Intrinsic Finite Element (VFIFE) Method," *Advances in Structural Engineering*, **17**, pp. 347-360 (2014).
33. Duan, Y. F. *et al*., "Vector Form Intrinsic Finite Element Analysis for Train and Bridge Dynamic In-

https://doi.org/10.1017/jmech.2017.85 Published online by Cambridge University Press

teraction," *Journal of Bridge Engineering* (In press).

34. Sáze, A., Gallego, R. and Domínguez, J., "Hypersingular Quarter-Point Boundary Element for Crack Problems," *International Journal for Numerical Methods in Engineering*, **38**, pp. 1681-1701 (1995).
35. Erdogan, F., "Stress Intensity Factors," *Applied Mechanics*, **50** (1983).
36. Fan, S. C., Liu, X. and Lee, C. K., "Enriched Partition-of-Unity Finite Element Method for Stress Intensity Factors at Crack Tips," *Computers and Structures*, **82**, pp. 445-461 (2004).
37. Duarte, C. A., "The Hp Clouds Method," Ph.D Dissertation, University of Texas, Austin, Texas, U.S. (1996).
38. Comite Euro-International du Beton, *CEB-FIP Mode Code 1990*, Thomas Telford Services Ltd, Thomas Telford House, Lausanne, Switzerland (1993).
39. Karihaoo, B. L. and Nallathambi, P., "Notched Beam Test: Mode I Fracture Toughness," *Fracture Mechanics Test Methods for Concrete*, pp. 1-86 (1991).

(Manuscript received March 30, 2017,
accepted for publication September 1, 2017.)

https://doi.org/10.1017/jmech.2017.85 Published online by Cambridge University Press